Journal of Power Sources 272 (2014) 1154–1161

Contents lists available at ScienceDirect

Journal of Power Sources

journal homepage: www.elsevier.com/locate/jpowsour

Degradation of lithium ion batteries employing graphite negatives and nickel–cobalt–manganese oxide + spinel manganese oxide positives: Part 2, chemical–mechanical degradation model

Justin Purewal [a, *], John Wang [a], Jason Graetz [a], Souren Soukiazian [a], Harshad Tataria [b], Mark W. Verbrugge [c]

[a] Sensors and Materials Laboratory, HRL Laboratories, LLC, Malibu, CA 90265, USA
[b] GM Vehicle Engineering, Global Battery Systems Engineering, Warren, MI 48092, USA
[c] GM R&D, Chemical and Materials Systems Lab, Warren, MI 48092, USA

HIGHLIGHTS

- A physics-based model is established to explain capacity fade in Li-ion cells.
- The model is consistent with the capacity fade trends observed in NCM + LMO/graphite cells.
- Fatigue crack growth in the graphite may be an important factor in the loss of usable lithium.

ARTICLE INFO

Article history:
Received 20 March 2014
Received in revised form
18 June 2014
Accepted 1 July 2014
Available online 22 July 2014

Keywords:
Capacity fade
Lithium-ion
NCM
LMO
Blended cathode
Fatigue

ABSTRACT

Capacity fade is reported for 1.5 Ah Li-ion batteries containing a mixture of Li–Ni–Co–Mn oxide (NCM) + Li–Mn oxide spinel (LMO) as positive electrode material and a graphite negative electrode. The batteries were cycled at a wide range of temperatures (10 °C–46 °C) and discharge currents (0.5C–6.5C). The measured capacity losses were fit to a simple physics-based model which calculates lithium inventory loss from two related mechanisms: (1) mechanical degradation at the graphite anode particle surface caused by diffusion-induced stresses (DIS) and (2) chemical degradation caused by lithium loss to continued growth of the solid-electrolyte interphase (SEI). These two mechanisms are coupled because lithium is consumed through SEI formation on newly exposed crack surfaces. The growth of crack surface area is modeled as a fatigue phenomenon due to the cyclic stresses generated by repeated lithium insertion and de-insertion of graphite particles. This coupled chemical–mechanical degradation model is consistent with the observed capacity loss features for the NCM + LMO/graphite cells.

1. Introduction

Lithium-ion batteries slowly lose capacity during cycling and storage. These capacity losses result from lithium inventory loss due to irreversible electrochemical side-reactions such as electrolyte reduction, and from loss of the active electrode materials due to particle isolation, phase transition, or other degradation mechanism [1,2]. Automotive applications require battery systems to maintain a sufficient performance for about ten years. Predicting the capacity losses that may occur over such a long time frame can be challenging. The standard approach is to perform accelerated aging tests where the battery is cycled or stored at a high temperature.

In Part 1 of this work [3] we described the results of an experimental study of capacity fade of NCM + LMO/graphite cells for a test matrix covering a broad range of temperature, discharge rate and discharge depth. A semi-empirical life model was established in Part 1 to account for the measured capacity fade. In the current work we build a physics-based model to better interpret the capacity fade that was measured. This approach can accelerate testing by reducing the number and length of battery life tests that are needed to extract important data.

Degradation mechanisms in lithium ion cells are modeled by methods ranging from semi-empirical fits of experimental data, to complex numerical simulations of the electrochemical side reactions. The semi-empirical approach relies upon curve fitting to

* Corresponding author. Tel.: +1 310 317 5626; fax: +1 310 317 5840.
E-mail address: jjpurewal@hrl.com (J. Purewal).

http://dx.doi.org/10.1016/j.jpowsour.2014.07.028
0378-7753/

large data sets and does not necessarily accelerate the testing process. In the numerical simulation approach, physical models for the degradation mechanisms are combined with the fundamental governing equations for the electrode to yield a set of partial differential equations. Such simulations require a detailed understanding of the specific material chemistry, which can be impractical for situations where the chemistry is not well understood.

To create a generalized and widely applicable model, we focus upon the dominant degradation mechanisms for composite graphite negative electrodes, which are present in nearly all commercial lithium ion batteries. Capacity fade at the graphite negative electrode is closely tied to the formation of a solid electrolyte interphase (SEI) film on the graphite surface, which can continue to grow slowly even after the initial cycles. Current evidence suggests that the SEI consists of both a dense, nonporous inner layer on the particle surface on the order of 20 nm–50 nm thick, and a porous outer layer which has a thickness of up to hundreds of nanometers. Growth of the SEI film with extended storage is often modeled as a diffusion-limited process, having a thickness growth that is approximately proportional to the square root of time (i.e., parabolic growth). In most electrochemical modeling studies of calendar loss and cycle loss, it is typically assumed that surface area covered by the SEI is uniform and unchanging [4]. However, as explained next, in situations where mechanical degradation of the electrode material is also an issue, changes in SEI area may also need to be taken into consideration.

Electrochemical cycling is known to increase [2] the rate of capacity loss (i.e., cycle loss) compared to open-circuit or constant voltage storage (i.e., calendar loss). Although the volume expansion for lithiated graphite is mild compared to lithium alloys, the repeated stresses may contribute to cycle loss through mechanical degradation at the negative electrode. Intercalation of lithium into graphite up to a stoichiometry of LiC_6 is accompanied by up to a 10% increase in the interlayer spacing. Repeated expansion and contraction generates diffusion-induced stresses (DIS), and can ultimately result in particle fatigue and crack propagation. The stress fields within a spherical electrode particle during lithium extraction, as calculated by linear elastic theory [5], are sufficiently large to promote fatigue cracking along existing defects. In terms of electrochemical capacity loss, useful lithium will be depleted by SEI formation on the newly exposed crack surfaces. Particle fracture and the electronic isolation of active electrode material are another effect of diffusion-induced stresses, although they are not considered in the present model.

Recent work has suggested that capacity fade models should address both chemical and mechanical degradation [6]. For cells with a lithium iron phosphate (LFP) cathode, a successful approach was to consider mechanical fatigue in graphite electrode particles under the repeated DIS during electrochemical cycling [7]. Mechanical fatigue was then correlated to crack growth on the particle surfaces, resulting in Li consumption by SEI formation on newly exposed crack surface. Motivation for this model was provided by experimental observation that capacity fade in the LFP cells was driven primarily by gradual lithium consumption through SEI growth on the negative electrode [8]. In this present work, we follow the approach of Deshpande et al. [7] to better understand the effect of both temperature and discharge rate on the capacity fade of NCM + LMO cells, guided by insights drawn from a large experimental test matrix.

We present experimental data collected for NCM + LMO commercial power cells containing a mixture of Li–Ni–Mn–Co layered oxide and Li–Mn oxide spinel as the positive electrode material. The negative electrode contains graphite as the active material. Electrochemical cycling was performed in accordance with a test matrix which examines the effects of calender life (t), cycle number (N), temperature (T), depth of discharge (DoD) and discharge rate (I_{cell}) on the capacity fade. Earlier cycle life and calendar life studies for the NCM + LMO cell chemistry covered a considerably smaller range of test conditions [9,10] The experimental data for NCM + LMO cells presented in Part 1 of this work point to lithium loss at the negative electrode as a dominant factor in the capacity loss during cycling, similar to results from an earlier study of LFP-graphite cells [6], The lithium loss is greatly accelerated at low temperature ($T = 10°C$) and fast discharge (7.5 A, 9.75 A) conditions, highlighting the important contribution of DIS to the capacity loss. A coupled chemical–mechanical degradation model originally reported in Ref. [7] is modified in the current work to address calender loss and variable discharge rate. This allows it to describe capacity fade over a wider range of operating conditions.

2. Experimental methods

Data was collected on commercially available 1.5 Ah 18650 cylindrical cells produced by Sanyo, a subsidiary of Panasonic. These cells have a blend of high capacity Li–Ni–Mn–Co oxide and high power Li–Mn oxide spinel as the cathode material, and have graphite as the anode material. Extensive details on the test matrix and test procedures are provided in Part 1 of this work (Ref. [3]). In defining the C-rates, a nominal capacity of 1.5 Ah was assumed.

Cycling was performed at four temperatures (10 °C, 22 °C, 34 °C and 46 °C) and five discharge rates (0.5C, 2C, 3.5C and 5C and 6.5C) were employed for cycle life testing. Cells cycled between an SOC of 1 and 0.5 (i.e., 50% DoD) were selected for modeling in this work. The cycle tests were performed between cutoff voltage of 4.2 V and 2.5 V. During cycling charging was performed at a 2C rate with one exception—for the 0.5C discharge samples, charging was performed at 0.5C. During the life cycle tests, cells were stopped at weekly intervals for characterization in which the capacity was measured by fully charging and discharging the cells at a 0.5C rate.

3. Model

3.1. Overview

Capacity loss at the negative electrode is modeled at the single particle level by considering only a graphite particle and omitting the other electrode components such as binder, conductive filler and other elements of porous electrodes. We assume that lithium loss is the capacity-limiting process for the NCM + LMO cells, an assertion which is supported by experimental data in the companion paper [3]. The depletion of useful lithium occurs through the continuous growth of an SEI layer on the graphite particle [11]. While in reality lithium may also be consumed in repairing the SEI layer (which can be damaged by volume expansion of lithiated graphite), we have not *directly* accounted for this in the model.

Numerical simulations of the SEI layer have yielded a power law dependence for the film thickness versus time, $L(t) - L(0) = Kt^{\gamma}$, where $\gamma \approx 0.5$ [12]. The observation that $\gamma \approx 0.5$ is consistent with a diffusion-controlled film growth of the SEI (i.e., parabolic growth). Models which take solvent diffusion through the SEI as the rate-limiting factor also yield a $\sim \sqrt{t}$ time dependence for the growth of the compact inner SEI layer thickness [13,14].

In general, test data at elevated temperatures corroborate a $\sqrt{t}$ correlation for calender loss (and presumably SEI thickness) [15,16]. Therefore, we model the increase in SEI layer thickness versus time by the following expression.

$$L_{SEI}(t) - L_{SEI}(0) = K_{th} t^{1/2} \quad (1)$$

where K_{th} is a temperature-dependent rate parameter and $L_{SEI}(0)$ is the initial SEI thickness following the cell formation cycle. It is emphasized, though, that this expression does not include the effect of voltage or electrolyte concentration on the SEI formation rate. Further, Eq. (1) does not differentiate between SEI formation during charge and discharge cycles. One would expect solvent reduction on graphite to occur primarily during the charging process.

3.2. Diffusion induced stress

Symmetric lithium diffusion into, and out of, a spherical particle of radius R is described by Fick's second law in spherical coordinates,

$$\frac{\partial C}{\partial t} = \frac{D}{r^2}\frac{\partial}{\partial r}\left(r^2\frac{C}{r}\right), \tag{2}$$

where C is lithium concentration and D is the lithium diffusion coefficient in Li_xC_6. With an uniform initial concentration of c_0, the solution for a galvanostatic boundary condition is given by

$$c(x,\tau) = c_0 + \frac{iR}{FD}\left[3\tau + \frac{1}{2}x^2 - \frac{3}{10} - \frac{2}{x}\sum_{n=1}^{\infty}\left(\frac{\sin(\lambda_n x)}{\lambda_n^2\sin(\lambda_n)}e^{-\lambda_n^2\tau}\right)\right] \tag{3}$$

where $x = r/R$ and $\tau = t/(R^2/D)$ [5]. The symmetric current density over the particle surface is denoted i, where negative currents correspond to discharge. The eigenvalues λ_n are the positive roots of $\tan(\lambda_n) = \lambda_n$. The current density i is estimated from the measured cell current by standard expression for sphere packing,

$$i = \frac{I_{cell}R}{3\varepsilon(AL)}, \tag{4}$$

where ε is the volume fraction of the solid phase within the negative electrode, A is the geometric electrode area, and L is the electrode thickness.

For composite graphite electrodes, $\varepsilon \approx 0.65$ is a reasonable value. Based on the nominal capacity (1.5 Ah) of the NCM + LMO cells, and an average energy density of 1.5 mAh cm^{-2}, we calculate an electrode area of $A = 1000\ cm^2$. The negative electrode thickness for the cells in this study was measured at 30 μm.

The evolution of stresses during galvanostatic discharge can be calculated from Eq. (3) by the stress–strain relationship for an isotropic, linear-elastic solid. The resulting expression in spherical coordinates for the tangential stress is.

$$\sigma_\theta = \frac{1}{3}\frac{E\Omega}{(1-\nu)}\frac{R^2}{FD}\frac{I_{cell}}{\varepsilon AL}\left[\frac{1}{5}\left(1-2x^2\right) + 2\sum_{n=1}^{\infty}\frac{e^{-\lambda_n^2\tau}}{\lambda_n\sin(\lambda_n)} \times \left(\frac{\sin(\lambda_n x)}{\lambda_n x} - \frac{\sin(\lambda_n x) - (\lambda_n x)\cos(\lambda_n x)}{\lambda_n^3 x^3}\right)\right], \tag{5}$$

where E is the Young's modulus, ν is the Poisson ratio, and Ω is the partial molar volume of the solute.

Since full lithium intercalation $6C + Li \rightarrow LiC_6$ results in a 10% volume expansion starting from an initial graphite density of 2.2 g cm^{-3}, we can estimate an effective average value for the lithium solute volume equal to $\Omega = 3.3\ cm^3\ mol^{-1}$. The Young's modulus and Poisson ratio for graphite are estimated as $E = 15$ GPa and $\nu = 0.27$. However, the Young's modulus may increase by up to a factor of three during Li intercalation [17]. A radius of $R = 5$ μm is assumed for the graphite particles in the negative electrode [18].

A diffusion coefficient of $D = 1 \times 10^{-13}\ m^2\ s^{-1}$ is used for Li diffusion in graphite between 10 °C and 46 °C. However, Li diffusivity in Li_xC_6 is strongly concentration dependent [19], varying by almost two orders of magnitude between $x = 0$ and $x = 1$. The tensile stress, given by Eq. (5), is plotted in Fig. 1 versus dimensionless time at several values of radial position r/R in the graphite particle. Negative values for stress denote compression.

The maximum tensile stress occurs at the particle surface, reaching a steady state value given by

$$\sigma_{\theta,max} = \frac{1}{45}\frac{E\Omega}{(1-\nu)}\frac{R^2}{FD}\frac{I_{cell}}{\varepsilon AL} \tag{6}$$

after roughly $\tau = 0.2$. The cross-over from tensile stress to compressive stress occurs at $x = 1/\sqrt{2}$, with compressive stress prevailing closer to the particle center. Based on the assumed particle radius and Li diffusion constant, the characteristic diffusion time constant is $R^2/D = 90$ s. In comparison, the time required for discharge from SOC = 1 to SOC = 0.5 is 900 s at 2C, and 277 s at 6.5C. Therefore, it is safe to assume that the steady state value for tensile stress in Eq. (5) is reached each discharge cycle. Values of $\sigma_{\theta,max}$ are plotted in Fig. 2 as a function of cell current I_{cell}.

3.3. Further elaboration on underlying assumptions

In the current model, graphite particles are treated as isotropic spherical particles within linear elastic theory. No distinction is made between the basal surfaces and prismatic (edge) surfaces of graphite, which have distinct properties in terms of Li intercalation, crack growth and SEI layer formation [20]. The anisotropic nature of graphite is also not included. In choosing our model parameters, we try to be consistent with the observed surface morphology and porous texture of typical graphite materials used in commercial Li-ion cells. Synthetic graphites often have a smooth surface along with a moderate mesoporous (2 nm–50 nm) structure, while natural graphites have greater surface roughness with little mesoporosity [21]. First cycle capacity loss is strongly correlated to the graphite surface area, so the N_2 BET specific surface areas (SSA) for commercial graphites will likely fall between 2 $m^2\ g^{-1}$ and 10 $m^2\ g^{-1}$ in order to keep first cycle losses below 10% [18].

We assume that the electrode manufacturing process (e.g., calendering) and formation cycle leaves the graphite particles with an initial density (ρ_{cr}) of sub-micron cracks on surface of the

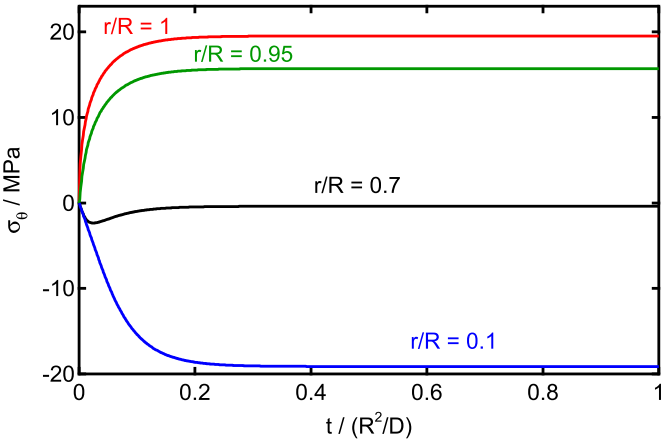

Fig. 1. Tangential stress during galvanostatic discharge at $I_{cell} = 9.75$ A (6.5C), plotted as function of dimensionless time, $\tau = Dt/R^2$, in units of MPa. Each trace corresponds to the stress evolution at a particular radial position, $x = r/R$. Positive values of σ_θ indicate tensile stress.

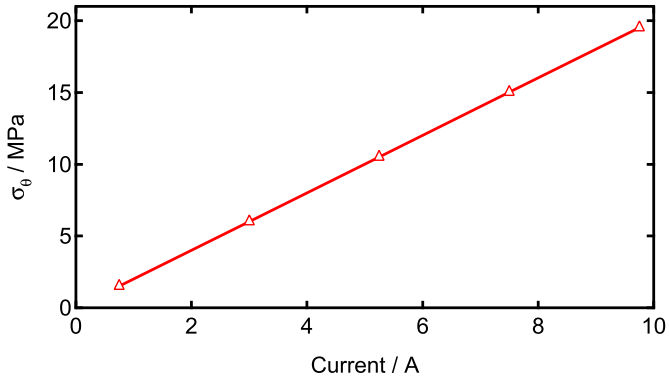

Fig. 2. Maximum tensile stress at the graphite particle surface plotted versus discharge current.

graphite electrode particle [22]. To be consistent with the observed mesoporosity of the synthetic graphites (i.e, no pores <2 nm) the width and length of the surface cracks are presumed to have an average value of 15 nm. Similarly we set the crack depth to an initial value of 20 nm. We assume that the density of cracks on the particle surface is 3 cracks per 1000 nm^2, which works out to $\rho_{cr} = 10^6$ cracks per 5 μm radius particle. With this crack density, approximately 70% of the spherical surface is occupied by cracks.

If we simply consider a graphite particle as a perfectly smooth spherical shape, the resulting SSA will be too small ($\ll 1\ m^2\ g^{-1}$). To match values for graphite surface areas, therefore, we choose a roughness factor of $r_{gr} = 13$ for the external surface of the graphite particle. The roughness factor in this case is the ratio of actual external surface area to the area of a smoothed envelope around the particle. By this approach, the initial external graphite surface area, excluding the contributions from cracks, works out to approximately 3.5 $m^2\ g^{-1}$. Cracked surfaces are also assumed to have a roughness factor of $r_{cr} = 13$. Much of this cracked surface area is likely to be created during the calendering step of manufacturing process or during the formation cycles [22], and therefore would not be reflected in the measured SSA's of the pristine material. Counting both the external and cracked surfaces of the graphite particle, the initial SSA is approximately 10 $m^2\ g^{-1}$, which is consistent with typical values for fabricated negative electrodes in commercial cells. This surface area is distinct from the value used in calculating the current density on the graphite particles in the negative electrodes, which assumes a smooth spherical surface.

The chemical composition of the SEI layer is not fully understood and it depends very strongly on the composition of the electrolyte [11]. It is known to be composite in nature and contains both inorganic and organic components. Inorganic compounds such as Li_2CO_3 are known to be one of the components of SEI films formed by reduction of ethylene carbonate. The proportionality between SEI thickness and Li consumption is estimated from well-known properties of commercial Li-ion cells. In particular, the BET N_2 surface area of negative electrodes in commercial cells is generally on the order of 10 $m^2\ g^{-1}$ even after electrode manufacturing. At the same time, the SEI layer on the negative electrode material following formation cycles is in the range of 20 nm–50 nm [14], and a value of 23 nm is assumed for this calculation.

It is well-known that graphite (365 mAh g^{-1}) typically consumes 10% of usable Li on the first cycle. For 1 g of graphite, a Li loss of 36.5 mAh (1.36 mmol Li) should be correlated to the formation of 10 m^2 × 23 nm=0.2 cm^3 of SEI. The proportionality constant is given by

$$V_{SEI} = \frac{1.362 \times 10^{-3}\text{moles Li}}{2 \times 10^{-7}\text{m}^3} = 6000\ \text{mol m}^{-3}, \tag{7}$$

which is considerably lower than the 57,000 mol m^{-3} for Li_2CO_3. The explanation for this is that the SEI also contains organic and polymeric specifies which do not contain Li.

Many electrolyte additives such as vinylene carbonate (VC) may polymerize to form polymeric components within and over the SEI layer [23]. Additives are likely used in all commercial cells due to their ability to extend cell life. Therefore, the mechanical fatigue properties of the SEI film are likely to be different from that of the host graphite. Mechanical properties of graphite do not change significantly within the narrow temperature range (10 °C–46 °C) that is explored in our measurements. On the other hand, some polymeric materials have a glass transition temperature within that range, and we would expect their mechanical fatigue properties to change significantly between 10 °C and 46 °C. The mechanical fatigue parameters that we include in the model may therefore be effective values that reflect an average of both graphite and the various SEI components. While mechanical degradation of the SEI layer itself is not explicitly included in our model, the fitted parameter values may implicitly reflect these effects.

3.4. Mechanical fatigue

During discharge, the tensile stress on the graphite particle reaches a steady-state value given by Eq. (6), and remains there for the remainder of the cycle. Lithium insertion during charge, on the other hand, produces compressive stresses at the particle surface. The repeated fluctuations between tensile and compressive stress near the particle surface creates mechanical fatigue, an ideal environment for crack growth. Three factors are necessary to cause fatigue: (1) a maximum tensile stress of sufficiently high value, (2) a large enough fluctuation in the applied stress, and (3) a sufficiently high number of cycles. Previous work has demonstrated that repeated Li intercalation and de-intercalation is sufficient to induce fatigue crack growth in graphite over a long period of continuous cycling [5,7].

Paris' Law is a well-known empirical expression for sub-critical crack growth caused by mechanical fatigue.

$$\frac{da}{dN} = k\Delta(K_I)^m \tag{8}$$

where a is the depth (from topmost surface) of the surface crack, and ΔK_I is the difference in mode I stress intensity factors for charge and discharge DIS. The constants k and m are inherently empirical, and can be treated as adjustable parameters in the current context. Although we treat them as fitting parameters in the model, k and m are related to material properties and should be dependent on the temperature, load frequency and other environmental factors. An edge crack in a large plate under uniaxial tensile stress has a stress intensity factor approximately equal to

$$K_I = \sigma_{\theta,\max} b\sqrt{\pi a}, \tag{9}$$

where $b = 1.12$ for small surface cracks ($a \ll R$). This expression is substituted into Eq. (8) to obtain the equation governing crack fatigue growth,

$$\frac{da}{dN} = k\left(\sigma_{\theta,\max} b\sqrt{\pi a}\right)^m \tag{10}$$

The solution to Eq. (10) for initial value $a(0) = a_0$ is given by

$$a = a_0\left(1 + \frac{2-m}{2}k\left[\sigma_{\theta,\max}b\sqrt{\pi}\right]^m a_0^{\frac{m-2}{2}}N\right)^{\frac{2}{2-m}}. \quad (11)$$

which describes the crack depth (a) as a function of cycle number (N).

An assumption made in this model is that the number of cracks on the graphite particle ($=4\pi R^2\rho_{cr}$) remains constant during cycling [7]. We also assume that the crack length and width remain fixed at $l_{cr} = 15$ nm, as described in Section 3.3. Therefore, only the depth a of the surface cracks increases with cycling. The proportionality constant between the crack depth and the total surface area contributed by the cracks is given by

$$A_{cr} = \left(4\pi R^2\rho_{cr}\right)(2l_{cr}r_{cr}), \quad (12)$$

where r_{cr} is the roughness factor. When the crack depth increases by an amount da, the newly exposed crack surface A_{cr}da is covered immediately by an SEI layer on the subsequent charge half cycle with thickness L_{SEI}^0. Lithium charge consumed per unit volume of SEI layer is equal to $V_{SEI}F$, where F is Faraday's constant and V_{SEI} was defined in Eq. (7) as the molar lithium concentration within the SEI.

The crack depth a increases with each succeeding cycle according to Eq. (8), and lithium is lost through SEI formation on the newly exposed crack surface. The amount of lithium consumed per cycle on the newly exposed crack surface area is then equal to $V_{SEI}FL_{SEI}^0(A_{cr}\mathrm{d}a/\mathrm{d}N)$. The lithium consumption by the first SEI layer on fresh crack surfaces, $(\mathrm{d}Q/\mathrm{d}N)_1$, is equal to

$$\left(\frac{\mathrm{d}Q}{\mathrm{d}N}\right)_1 = V_{SEI}FL_{SEI}^0A_{cr}\left[\sigma_{\theta,\max}b\sqrt{\pi a_0}\right]^m k \times \left(1 + \frac{2-m}{2}k\left[\sigma_{\theta,\max}b\sqrt{\pi}\right]^m a_0^{\frac{m-2}{2}}N\right)^{\frac{m}{2-m}}. \quad (13)$$

3.5. Calendar loss

The formation cycle produces an SEI film which we assume to cover the entire spherical particle surface with a thickness L_{SEI}^0. With each succeeding cycle, we assume that a new layer is deposited on top of the initial SEI film. The total area of the initial SEI film is equal to the combined area of the particle surface and surface cracks.

$$A_{SEI}^0 = 4\pi R^2 r_{gr} + A_{cr}a_0, \quad (14)$$

where r_{gr} is the roughness factor for external graphite surfaces. The amount of lithium consumed by the increase in thickness of the initial SEI layer during cycle N is given by,

$$Q_{SEI}(N) = V_{SEI}FA_{SEI}^0[L_{SEI}(N) - L_{SEI}(N-1)], \quad (15)$$

where $\mathrm{d}L_{SEI}/\mathrm{d}N \approx L_{SEI}(N) - L_{SEI}(N-1)$ is the incremental change in SEI thickness for cycle N. Based on Eq. (1), the increase in SEI film thickness follows a square root of time dependence. The amount of lithium consumed with each successive cycle is therefore

$$\left(\frac{\mathrm{d}Q}{\mathrm{d}N}\right)_2 = V_{SEI}FA_{SEI}^0\left(\frac{K_{th}}{2\sqrt{t}}\right)\left(\frac{\mathrm{d}t}{\mathrm{d}N}\right). \quad (16)$$

Eq. (16) describes the total lithium loss per cycle, $(\mathrm{d}Q/\mathrm{d}N)_2$, due to increase in thickness of the original SEI layer. The time varies approximately linearly with cycle number, and $(\mathrm{d}t/\mathrm{d}N)$ is therefore the slope of the elapsed time versus total cycles.

3.6. Growth of SEI films on the cracked surfaces

For completeness, it is assumed that the SEI films deposited on newly cracked surfaces continue to increase during succeeding cycles. (A simpler and less accurate approach would be to assume that the SEI grows immediately to its final thickness during the cycle in which the crack area is exposed.) If the current cycle is N, and we consider a patch of crack surface formed during any previous cycle i, the SEI layer on that patch will have grown during the ensuing $N-i$ cycles. During cycle N, therefore, the total lithium consumption by SEI increase on patches formed during previous cycles ($1 < i < N$) is equal to

$$\left(\frac{\mathrm{d}Q}{\mathrm{d}N}\right)_3 = V_{SEI}F\sum_{i=1}^{N-1}\left(A_{cr}\frac{\mathrm{d}a}{\mathrm{d}N}\right)_i\left(\frac{\mathrm{d}L_{SEI}}{\mathrm{d}N}\right)_{N-i}. \quad (17)$$

Referring back to Eq. (13) for $(A_{cr}\mathrm{d}a/\mathrm{d}N)$ and to Eq. (16) for $(\mathrm{d}L_{SEI}/\mathrm{d}N)$, the expression in Eq. (17) can be written out as

$$\left(\frac{\mathrm{d}Q}{\mathrm{d}N}\right)_3 = V_{SEI}F\sum_{i=1}^{N-1}A_{cr}k\left[\sigma_{\theta,\max}b\sqrt{\pi a_0}\right]^m \times \left(1 + \frac{2-m}{2}k\left[\sigma_{\theta,\max}b\sqrt{\pi}\right]^m a_0^{\frac{m-2}{2}}i\right)^{\frac{m}{2-m}} \times \frac{K_{th}}{2}(N-i)^{-1/2}\left(\frac{\mathrm{d}t}{\mathrm{d}N}\right). \quad (18)$$

This term reflects the coupled effect of chemical and mechanical degradation.

The total capacity loss per cycle for a single graphite particle equals the sum of Eqs. (13), (16) and (18),

$$\left(\frac{\mathrm{d}Q}{\mathrm{d}N}\right) = \left(\frac{\mathrm{d}Q}{\mathrm{d}N}\right)_1 + \left(\frac{\mathrm{d}Q}{\mathrm{d}N}\right)_2 + \left(\frac{\mathrm{d}Q}{\mathrm{d}N}\right)_3. \quad (19)$$

However, for comparison to the measured capacity loss, Eq. (19) must be expressed as a fraction of the nominal capacity of the as-received commercial cells. To calculate the *fractional* capacity loss predicted by the model, the initial capacity of a single graphite particle (following formation cycle) needs to be estimated. Assuming a formation cycle efficiency of $\eta_{fc} = 0.9$ and a graphite specific capacity of 365 mAh g^{-1}, the capacity at the start of cycling is

$$Q_0 = \eta_{fc}\left(365\ \mathrm{mAh\ g^{-1}} \times \frac{4}{3}\pi R^3\rho_{gr}\right), \quad (20)$$

where $\rho_{gr} = 2.25$ g cm^{-3} is the density of graphite.

4. Results and discussion

The cumulative capacity loss versus cycle number, as predicted by the model, was determined by numerically integrating Eq. (19) (which gives the capacity loss per cycle). The Paris' law constants k and m, and the SEI layer rate constant K_{th} were treated as adjustable parameters, and were fitted to measured data by a constrained non-linear optimization routine in MATLAB. A single global value of $m = 2.2$ was used for all temperatures and discharge rates. On the other hand, k and K_{th} were allowed to vary with temperature. The fit results for the 10 °C and 46 °C data are shown in Figs. 3 and 4, respectively. Fitted values for m, k and K_{th} are summarized in Table 1. The experimental NCM + LMO capacity loss is normalized with respect to the cell capacities measured before the first cycle (Q_0).

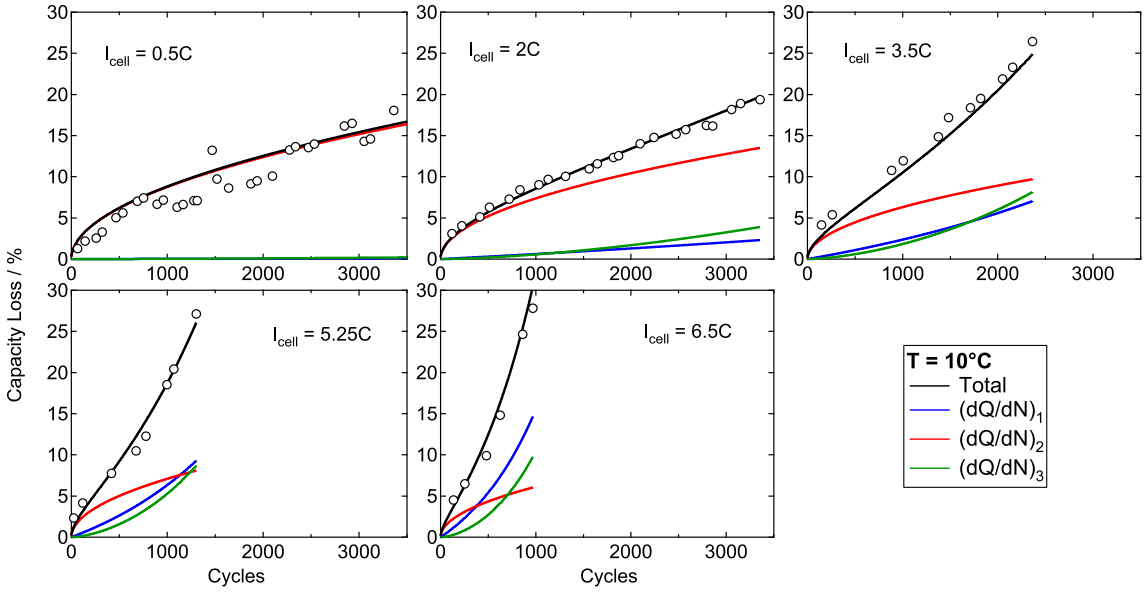

Fig. 3. Capacity fade data for NCM + LMO cells cycled at 10 °C and discharge rates between 0.5C and 6.5C. Solid black lines indicate the total capacity loss calculated from Eq. (19), while the blue, red and green lines represent the relative contributions of the crack growth (Eq. (13)), SEI layer growth (Eq. (16)) and SEI layer growth on cracked surfaces formed during previous cycles (Eq. (18)), respectively. The model is calculated from parameters listed in Table 1. (For interpretation of the references to color in this figure legend, the reader is referred to the web version of this article.)

As shown in Fig. 3, the dominant lithium loss mechanism at low temperature and high discharge rate is crack propagation, $(dQ/dN)_1$, combined with SEI formation on newly exposed graphite surfaces. At 46 °C, however, growth of the existing SEI layer, $(dQ/dN)_2$, appears to be the dominant mechanism for capacity loss—consistent with commonly observed behavior. A closer examination of the SEI thicknesses and surface crack depths predicted by this model provides a coherent picture of negative electrode degradation during extended electrochemical cycling.

Based on the assumption of 90% formation cycle efficiency, the initial SEI layer thickness is $L^0_{SEI} \approx 23$ nm. The final SEI thickness varies depending on the temperature and discharge current. For cells cycled at 46 °C/0.5C conditions, the predicted SEI thickness is 100 nm after roughly 1900 cycles. On the other hand, at 10 °C/0.5C cycling the predicted SEI thickness is only 60 nm after more than 3500 cycles. In comparison, experimental measurements of the initial SEI thickness in LMO/graphite cells were on the order of 40 nm, which increased to nearly 400 nm after storage for 1 year at 40 °C [14].

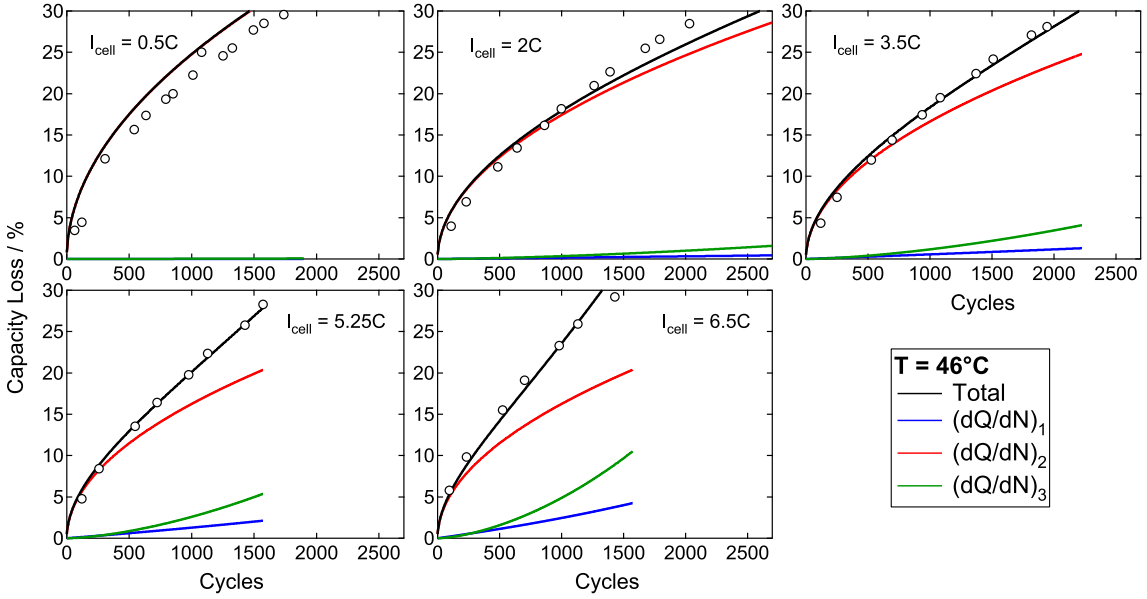

Fig. 4. Capacity fade data for NCM + LMO cells cycled at 46 °C and discharge rates between 0.5C and 6.5C. Solid black lines indicate the total capacity loss calculated from Eq. (19), while the blue, red and green lines represent the relative contributions of crack growth (Eq. (13)), the SEI layer growth (Eq. (16)) and SEI layer growth on cracked surfaces formed during previous cycles (Eq. (18)), respectively. The model is calculated from parameters listed in Table 1. (For interpretation of the references to color in this figure legend, the reader is referred to the web version of this article.)

Table 1
Fitted values for model parameters.

T °C	$k/10^{-20}$	$K_{th}/10^{-10}$	m
10	13.6	16.2	2.2
22	3.9	18.2	2.2
34	2.5	25.4	2.2
46	3.6	45.1	2.2

In Section 3.3 we assumed that there was a fixed population of cracks (10^6) on a single graphite particle (possibly formed during manufacturing and formation cycling), each having a uniform initial crack depth of 20 nm. The increase in crack depth that is predicted by the model, as expected, is largest at 10 °C and at high discharge rates. At 10°C/6.5C conditions, the final crack depth is 65 nm after 1000 cycles. In contrast, the crack depth does not change appreciably up to 2000 cycles for cells cycled at 0.5C rate at any of the measured temperatures.

Based on the values of initial crack depth (a_0), particle size (R) and initial crack density (ρ_{cr}) listed in Table 2, the initial graphite surface area is roughly 10 $m^2\ g^{-1}$ (see Section 3.3). For the 10°C/6.5C cycling conditions (which generated the deepest cracks) the surface area is more than doubled, with a value of 25 $m^2\ g^{-1}$ at 1000 cycles. These surface areas are within the range observed for synthetic graphites [20,18,24].

Of the three adjustable parameters included in this model, two of them (k, K_{th}) exhibited variation with temperature. Fitted values of the fatigue parameter k are plotted versus temperature in Fig. 5. The value of k is on the order of 1×10^{-20}, increasing sharply as the temperature is lowered to 10 °C. This strong temperature dependence is inconsistent with the known mechanical properties of graphite, which does not show any transitions between brittle and ductile phases near 10 °C.

One possible explanation for this anomalous temperature variation of k is that it is implicitly parameterizing other phenomena, such as the mechanical degradation of the SEI layer itself. If the SEI layer were to deform and crack during electrochemical cycling, usable Li would be consumed in repairing the SEI layer. As noted in Section 3.3, many electrolyte additives such as VC can be reduced to form polymer-like components embedded within the composite SEI structure. Since certain polymers have a brittle-to-elastic glass transition temperatures around 10 °C, and consequently exhibit large changes in the mechanical fatigue behavior, this would be consistent with the steep rise in k at that temperature. Based on the information we currently have, it does not appear possible to separate the cracking of graphite active material from cracking of the SEI layer.

Table 2
List of parameters.

Symbol	Description	Value	Units
A	Geometric area of electrode	1000	cm^2
a_0	Initial crack depth	20	nm
D	Li diffusion coefficient	1×10^{-13}	$m^2\ s^{-1}$
E	Young's modulus of graphite	15	GPa
L	Electrode thickness	30	μm
l_{cr}	Crack length, width	15	nm
m	Paris' law exponent	2.2	
R	Radius	5	μm
V_{Li}	Li concentration in SEI	6000	$mol\ m^{-3}$
ε	Solid phase porosity	0.65	–
η	Formation cycle efficiency	0.9	–
ρ_{cr}	Cracks per 1000 nm^2	3.18	$10^{-3}\ nm^{-2}$
Ω	Partial molar volume of solute	3.3	$cm^3\ mol^{-1}$
ν	Poison ratio	0.27	–
–	Graphite capacity	365	$mAh\ g^{-1}$

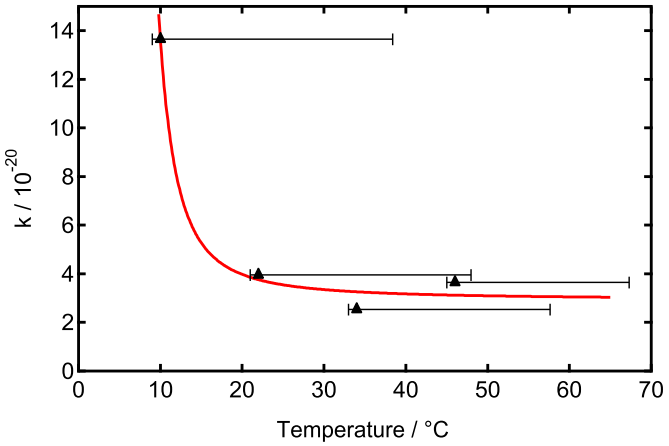

Fig. 5. Fitted values for the Paris' law constant k plotted versus temperature. Solid line is included as a guide. The $+x$ error bars indicate the maximum temperature excursions of the cells during 6.5C discharge.

The rate constant for SEI layer growth, K_{th}, is plotted versus temperature in Fig. 6. The temperature dependence of K_{th} is consistent with the Arrhenius equation, with an activation energy $E_a = 21.2$ kJ mol^{-1} and pre-factor $K_{th,0} = 1.1 \times 10^{-5}$. This is consistent with a thermally activated chemical reaction rate for SEI formation. Further, this activation energy is similar to the value (24.5 kJ mol^{-1}) that is obtained in Part 1 of this work by using an empirical fitting approach [3].

A major assumption made in this analysis is that the cell temperature remains equal to the temperature of the environmental test chamber. During rapid discharges, however, the internal temperature of the cells can rise by 20 °C or more, followed by a cool-down when the battery is recharged at a moderate rate. To test this assumption we monitored the external battery temperature during 6C discharge. The results (shown in the Supporting information, Fig. SI1) indicate that cells in a 22 °C environment can rapidly heat to 50 °C during a 6C discharge. Similarly, cells in a 50 °C environmental chamber heat up to 75 °C during 6C discharge. The *internal* cell temperatures should likely exhibit even larger

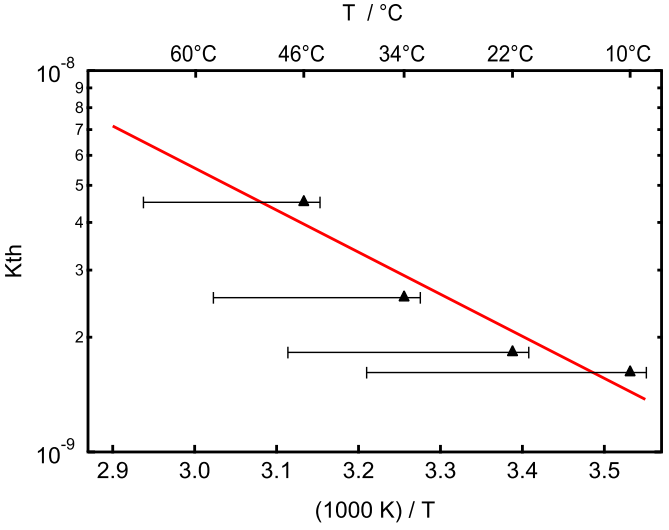

Fig. 6. Fitted values for the rate constant for SEI layer growth, K_{th}, plotted versus temperature. The solid line represents the best-fit to the Arrhenius equation. The $-x$ error bars indicate the maximum temperature excursions of the cells during 6.5C discharge.

temperature spikes than those measured on the outer surface by thermocouple probes.

The primary impact of these cyclic thermal fluctuations should be on the reaction kinetics of the SEI formation, which would speed up during the high T intervals. Therefore, the K_{th} values listed in Table 1 may actually correspond to effective temperature-averaged values. In Figs. 5 and 6 we include error bars in the $+x$ direction to indicate the maximum temperature excursions experienced by the NCM + LMO cells (at 6.5C).

Agreement between NCM + LMO cycling data and the chemical–mechanical degradation model provides strong, if indirect, support for the importance of fatigue cracking and mechanical degradation towards overall cell capacity fade. The validity of this model hinges upon gradual changes in the surface morphology and crack growth of graphite particles in response to extensive electrochemical cycling. To date, however, there do not appear to have been any quantitative studies of graphite cracking and surface morphology during repeated Li intercalation.

In Part 1 of this work [3], we provide a detailed differential voltage analysis that supports our assumption that lithium loss is the dominant cause of capacity fade in the NCM + LMO cells. From the shifts and spacing between the characteristic dV/dQ peaks of lithiated graphite, it is determined that Li loss outpaces both cathode material loss and anode material loss as the capacity-limiting factor in almost all the tested NCM + LMO/graphite cells. However, this provides only indirect support for fatigue cracking and coupled chemical–mechanical degradation. Direct imaging studies of graphite particles [25] and cathode materials [26] following electrochemical cycling have found evidence of crack formation and propagation, but there is no way to correlate this to a change in the overall graphite surface area. At the same time, previous results have demonstrated that the BET surface area of graphite particles can be increased more than four-fold by mechanical milling [20]. In this context, the two-fold increase in surface area through fatigue crack growth predicted here appears plausible.

5. Conclusion

Capacity fade in lithium-ion battery with a blended Li–Ni–Co–Mn oxide and Li–Mn spinel positive electrode was studied in cells cycled across a range of temperatures (10 °C–46 °C) and discharge currents (0.5C–6.5C). The experimental data was described by a single particle model which combines two mechanisms for lithium loss in the NCM + LMO cells: (1) fatigue crack growth at the graphite particle surface from repeated diffusion-induced stresses, (2) growth of the SEI film thickness under diffusion-limited chemical kinetics. This dual degradation model accurately predicts capacity loss across wide ranges of operating temperature and discharge current, while simultaneously providing an intuitive physical picture of degradation at the negative electrode.

Appendix A. Supplementary data

Supplementary data related to this article can be found at http://dx.doi.org/10.1016/j.jpowsour.2014.07.028.

References

[1] J. Vetter, P. Novak, M. Wagner, C. Veit, K. Möller, J. Besenhard, M. Winter, M. Wohlfahrt-Mehrens, C. Vogler, A. Hammouche, J. Power Sources 147 (2005) 269–281.
[2] R. Spotnitz, J. Power Sources 113 (2003) 72–80.
[3] J. Wang, et al., Macromolecules (2014). http://dx.doi.org/10.1016/j.jpowsour.2014.07.030.
[4] M. Pinson, M. Bazant, J. Electrochem. Soc. 160 (2013) A243–A250.
[5] Y. Cheng, M. Verbrugge, J. Power Sources 190 (2009) 453–460.
[6] J. Wang, P. Liu, J. Hicks-Garner, E. Sherman, S. Soukiazian, M. Verbrugge, H. Tataria, J. Musser, P. Finamore, J. Power Sources 196 (2011) 3942–3948.
[7] R. Deshpande, M. Verbrugge, Y. Cheng, J. Wang, P. Liu, J. Electrochem. Soc. 159 (2012) A1730–A1738.
[8] P. Liu, J. Wang, J. Hicks-Garner, E. Sherman, S. Soukiazian, M. Verbrugge, H. Tataria, J. Musser, P. Finamore, J. Electrochem. Soc. 157 (2010) A499–A507.
[9] J. Belt, V. Utgikar, I. Bloom, J. Power Sources 196 (2011) 10213–10221.
[10] M. Dubarry, C. Truchot, B.Y. Liaw, K. Gering, S. Sazhin, D. Jamison, C. Michelbacher, J. Power Sources 196 (2011) 10336–10343.
[11] M. Winter, Z. Phys. Chem. 223 (2009) 1395–1406.
[12] J. Christensen, J. Newman, J. Electrochem. Soc. 151 (2004) A1977–A1988.
[13] H. Ploehn, P. Ramadass, R. White, J. Electrochem. Soc. 151 (2004) A456–A462.
[14] T. Yoshida, M. Takahashi, S. Morikawa, C. Ihara, H. Katsukawa, T. Shiratsuchi, J.-I. Yamaki, J. Electrochem. Soc. 153 (2006) A576–A582.
[15] I. Bloom, B. Cole, J. Sohn, S. Jones, E. Polzin, V. Battaglia, G. Henriksen, C. Motloch, R. Richardson, T. Unkelhaeuser, D. Ingersoll, H. Case, J. Power Sources 101 (2001) 238–247.
[16] M. Broussely, Advances in Lithium-ion Batteries, Kluwer Academic/Plenum Publishers, 2002, pp. 393–431.
[17] Y. Qi, H. Guo, L. Hector, A. Timmons, J. Electrochem. Soc. 157 (2010) A558–A566.
[18] D. Aurbach, H. Teller, E. Levi, J. Electrochem. Soc. 149 (2002) A1255–A1266.
[19] M. Verbrugge, B. Koch, J. Electrochem. Soc. 150 (2003) A374–A384.
[20] J.P. Olivier, M. Winter, J. Power Sources 97 (2001) 151–155.
[21] F. Joho, B. Rykart, A. Blome, P. Novák, H. Wilhelm, M.E. Spahr, J. Power Sources 97 (2001) 78–82.
[22] D. Liu, Y. Wang, Y. Xie, L. He, J. Chen, K. Wu, R. Xu, Y. Gao, J. Power Sources 232 (2013) 29–33.
[23] L. El Ouatani, R. Dedryvere, C. Siret, P. Biensan, D. Gonbeau, J. Electrochem. Soc. 156 (2009) A468–A477.
[24] J. Arrebola, A. Caballero, L. Hernán, J. Morales, J. Electrochem. Soc. 156 (2009) A986–A992.
[25] S. Bhattacharya, A.R. Riahi, A.T. Alpas, J. Power Sources 196 (2011) 8719–8727.
[26] D. Chen, Microscopic Investigations of Degradation in Lithium-ion Batteries (Ph.D. thesis), Karlsruher Institut für Technologie (KIT), 2012.